DOI: 10.15480/882.9357

Eighth International Symposium on Marine Propulsors
smp'24, Berlin, Germany, March 2024

Multi-Fidelity Modeling for Waterjet Propelled High Speed Small Craft

Christian Milano, Zhaoyuan Wang, Sungtek Park, Frederick Stern

IIHR—Hydroscience & Engineering, The University of Iowa, Iowa City, Iowa, USA

ABSTRACT

In the present study, multi-fidelity modeling of the Delft catamaran is performed including captive, self-propulsion, and prescribed trim and sinkage simulations. High-fidelity simulations are conducted first to verify the computational setup and validate the computational results. A low-fidelity force and moment propulsion model is implemented based on the high-fidelity simulation results and a hydrostatic correlation, which is applied to self-propulsion simulations. The low-fidelity propulsion model trained based on the high-fidelity computational data shows better simulation results (errors less than $5\%D$) than using the hydrostatic correlation. The computations are accelerated by a factor up to 8 using the low-fidelity model. Issues for the computational setup including center of gravity, displacement with waterjet system, pump curve, and waterjet flow analysis methods are also addressed. Future work will be focused on the waterjet propelled Generic Prismatic Planing Hull (GPPH) and extending the analysis to maneuvering conditions.

Keywords

Waterjet, Delft catamaran, multi-fidelity, CFD, high-speed small craft.

1 INTRODUCTION

Waterjet (WJ) propulsion for ships uses pumps to generate thrust, which is known for its increased maneuverability, reduced maintenance requirements, shallow water capability, and enhanced safety as compared to the traditional propellers. The WJ propulsion represents an optimal choice for high-speed ships and small craft, however, the complexity of the experimental and numerical analysis methods has been an obstacle to their design and realization of full performance potential.

The experimental analysis methods rely on the ITTC (Van Terwisga 2005) waterjet test procedure control volume method, which is difficult to implement, with a large scatter in test outcomes. Only limited numerical analysis methods have been developed and mostly with substantial approximations concerning both geometry and conditions. A collaborative effort between IIHR, BSHC, CNR-INM, and NMRI (Kandasamy et al 2013) has been focused on simulation-based design for the waterjet propelled Delft Catamaran (DC), including integrated experiments and variable fidelity computations using CFD, potential flow, and Reduced-order Models (RoM) (Kandasamy et al 2010). The high-fidelity optimization achieved a 4% reduction in bare hull resistance and 11% reduction in effective pump power for self-propulsion. Subsequent collaboration between IIHR (CFD and experiments) and BSHC (system-based and experiments) for the DC maneuvering and course stability in calm water showed limitations of both prediction methods, which were attributed to deficiencies in waterjet modeling for nozzle deflection conditions (Milanov et al 2014; Sadat-Hosseini et al 2013; Stocker et al 2014). Recently, Zou et al (2023) used the experimental data from this effort for the validation of their DC bare hull and waterjet self-propulsion CFD. Dogan et al (2022) compared both control volume and integral analysis methods in the investigation of the effects of hook, interceptor, and waterjets on the Littoral Combat Ship (LCS) resistance/power, sinkage, and trim, including model and full-scale validation.

CFD simulations of WJ propelled craft are computationally expensive and difficult due to the complex geometries of the WJ system, especially when a movable nozzle is included for the maneuvering. An integral force/moment WJ model is developed by Kandasamy et al (2010) with an alternative control volume including vertical forces and pitching moment. A maneuvering model based on CFD methods (Sadat-Hosseini et al 2013) has been developed using a body-force impeller defined by pump curves with various slopes, which have been applied to the simulations of turning circles and zig-zag maneuvers. As mentioned previously both models show limitations, and the RoM is still not fully developed.

The present research builds on previous IIHR research as described above with the objective of developing robust and accurate multi-fidelity capability, including RoM, for use in the digital design of high-speed small craft (Stern et al 2022). The high-fidelity CFD solver, CFDShip-Iowa, will be combined with the capabilities of multi-fidelity modeling to generate a reduced cost simulation framework for WJ propelled small craft. The model will be trained using DC data and subsequently extended to the Generic Prismatic Planing Hull (GPPH) (Stern et al 2022), to verify its use for digital design.

The single-phase flow solver, CFDShip-Iowa V4.5, is used for the CFD simulations, which include captive, self-propulsion, and prescribed trim and sinkage conditions. The self-propulsion simulations are carried out for two fidelity levels, namely, high-fidelity (HF) and low fidelity (LF, i.e., RoM). For the HF simulations, the geometries of the hull and WJ systems (tube and nozzle) with a body-force model (Kandasamy et al 2013) for the pump impellers are used. In the LF simulations, only the bare hull geometry is used with a set of point-forces and moments implemented to consider the thrust and WJ-hull interaction (Kandasamy et al 2010).

2 EXPERIMENTAL STUDIES

The geometry used in the experiments is the DC model 372 designed at Delft University of Technology (Van't Veer 1998). The hull is propelled by two waterjet units and the design speed is $Fr = 0.5$. The hull geometry is shown in Figure 1 and the principal parameters of the DC can be found in the recent study (Zou et al 2023). The experiments have been carried in both BSHC (Milanov 2010) and INSEAN (Miozzi 2011) with three setups including bare hull test, bollard pull test, and self-propulsion test.

In the bare hull tests, both the intake and nozzle are closed, and the resistance, sinkage, trim, static pressure, and boundary layer velocity profiles on the center line of the hull are measured. In the bollard pull test, the pumps are operated within a specific range of impeller revolutions with both intake and nozzle open. The bollard pull force (the thrust generated by both water-jet pumps), the reference dynamic pressure at the waterjet nozzle exit, the jet velocity at the nozzle exit, and the impeller's revolutions per second (RPS) are measured. The flow rate is also determined through direct measurement by weighing the collected water and estimated using the concept of momentum flux. In the self-propulsion test, thrust and torque generated by the waterjet shaft are measured, together with its rotational speed, the carriage velocity, the reference dynamic pressure at the nozzle exit, as well as the model's sinkage and trim. The waterjet thrust performance, delivered power, and waterjet flow rate are also reported.

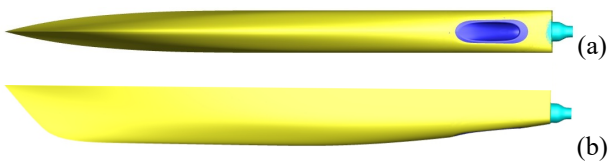

Figure 1: Geometry of the DC with water-jet propulsion system: (a) bottom view, (b) side view.

3 COMPUTATIONAL METHODS, SETUP, AND ANALYSIS METHODS

3.1 Mathematical Model and Numerical Method

CFDShip-Iowa V4.5 (Huang et al 2008) is used for the CFD studies. The incompressible Reynolds Averaged Naiver-Stokes (RANS) equations are solved in CFDShip-Iowa. All variables and fluid properties are non-dimensioned with the reference velocity U and ship length L. A single-phase level set method (Carrica et al 2007a) is used for the free surface modeling in V4.5. The pressure in the air region is constant, and the zero normal gradient for both the k and ω are used at the free surface. Periodic reinitializations of the level set function are performed to keep the property of being a distance function during the simulation. The Menter's blended $k-\omega/k-\epsilon$ turbulent model (Menter 1994) is used for turbulence modeling. The 6DoF motion of ships is predicted by solving the rigid body equations of motion and is realized using the overset grid technique. Suggar (Noack 2005) is used to obtain the overset domain connectivity information for overlapping grids. The details of the implementation can be found in (Carrica et al 2007b). The PID controller is used for the propeller or water-jet steering angle to keep the target speed or coarse keeping, respectively.

An implicit second-order Euler backward difference scheme is used for the time derivatives. The convection terms can be discretized using the 1st or 2nd order upwind, 3rd order QUICK, and 4th order upwind schemes, and the 2nd order central difference scheme is used for the diffusion terms. The same discretization schemes are used for the turbulence and level set equations. Incompressibility is enforced by a strong pressure/velocity coupling using a Projection (fractional time step) method (Bell et al 1991; Huang et al 2007), and the resulting pressure equation is solved using the Portable Extensible Toolkit for Scientific Computing (PETSc) toolkit. The code is parallelized using the MPI-based domain decomposition approach, where each decomposed block is mapped to one processor. Details of the mathematical models and numerical methods can be found in the above papers and references therein.

3.2 Multi-Fidelity Modeling for Waterjet Propulsion

Both the high- and low-fidelity waterjet propulsion models are used for the self-propulsion simulations. The low-fidelity models are trained using the high-fidelity CFD data.

3.2.1 High-Fidelity Simulations

For the high-fidelity simulations, both geometries of the hull and waterjet system (including intake, duct, and nozzle) are considered. The waterjet impeller is modeled as a body force based on an axisymmetric body force model (Stern et al 1988), which includes axial and tangential components with a radial distribution depending on the advance coefficient J. In this model, impeller blade tip loading and tip clearance flow are not considered. For waterjet pumps, the tangential forces are set to be zero to simulate the straightening effect of the stator blades, and the impeller hub and shaft are not modeled. The selection of an axisymmetric body force model might influence flow inhomogeneity, particularly due to potential non-uniform inflow on the impeller working inside the waterjet channel downstream from the inlet. Further investigation into this matter is needed. The K_t curve is provided as a second-order polynomial fit derived from the experimental pump curve. This curve is constructed using data obtained from

thrust, revolutions per second (RPS), and ship speed measured in the bollard and self-propulsion experimental tests, as shown in Figure 2. It should be noted that the experimental data are only available for high J values (0.8), and the J value used in the present simulations is around 0.61. As will be shown later, the impeller RPS is overpredicted by 30.21% compared to the EFD data. The overprediction of both the flow rate and RPS is also reported by Sadat-Hosseini et al (2013). Further experiments are required to collect data for low J conditions and construct a more accurate functional form for the pump curve. As for maneuvering, it is important to understand the impact of the turning nozzle on pump performance, as there is a lack of information in the maneuvering experiments.

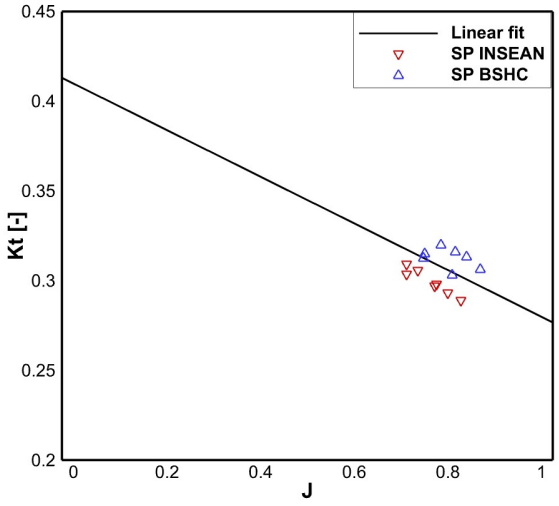

Figure 2: EFD data for pump performance and linear fit used in CFD simulations.

3.2.2 Low-Fidelity: Hydrostatic and Direct Models

The hydrostatic model for the waterjet induced changes in sinkage and trim is based on the hydrostatic approximations by Kandasamy et al (2010). The increment in heave can be written as:

$$\Delta\sigma = F_Z/\rho g A_{WP} \tag{1}$$

where $\Delta\sigma$ is the induced sinkage due to the waterjet, A_{WP} is the hull waterplane area, and ρ is the density of the water. The increment in trim is expressed as:

$$\Delta\tau = M_{WJ}/\rho g I_L \tag{2}$$

where $\Delta\tau$ is the waterjet induced change in trim angle and I_L is the longitudinal moment of inertia about the center of flotation. Once the high-fidelity captive and self-propulsion simulations are completed, $\Delta\sigma$ and $\Delta\tau$ are known. Therefore, these formulas can be used to obtain the values of F_Z and M_{WJ} that need to be applied on the bare hull for the self-propulsion simulations.

For the direct model, vertical force (F_Z) and pitch moment (M_{WJ}) are obtained from additional CFD simulations with prescribed sinkage and trim predicted using the high-fidelity simulations.

F_z and M_{WJ} are then applied to the bare hull along with a point force F_x, as shown in Figure 3. The point force F_x is a simplified model of the impeller thrust and is adjusted by a PID controller. The F_z, M_{WJ}, and F_x represent the forces and moments induced by the waterjet on the hull. F_x can be correlated to the self-propulsion delivered power using the waterjet efficiency η_D.

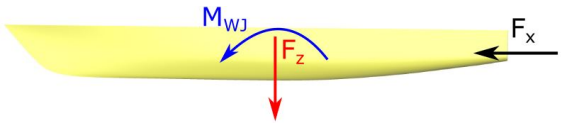

Figure 3: Point forces and pitch moment applied to the bare hull in the low-fidelity models.

3.3 Computational Setup and Flow Conditions

3.3.1 Captive Simulation Setup

For captive simulations, only the hull geometry is used. The computational domain of $x/L = [-1.2, 4.0]$, $y/L = [0, 2]$, and $z/L = [-0.39, 0.67]$ is used with a Cartesian background and body-fitted overset grids shown in Figure 4. The total number of grid points is given in Table 1. The boundary layer of the hull surface grid is designed to achieve $y^+ < 1$. Note that the half body grid is used for all simulations. A systematic grid verification study is not conducted. However, this is particularly important for critical areas such as the waterjet inlet and outlet, the stern wave area, and the domain between the catamaran hulls where interaction between the wave systems of the two hulls takes place. These issues will be addressed in future work. A time step of 0.002s is used with an average CFL number of 0.8 at the highest ship speed corresponding to Fr=0.7. No-slip wall boundary condition is imposed on the surface of the hull. Uniform inflow condition is applied at the inlet and zero second derivative of velocity is used for the outlet. Zero gradient boundary conditions are used at one side of the domain, and the symmetry boundary condition is used at the center plane. Far field boundary conditions are applied at the top and bottom of the domain. The pivot point is positioned above the center of gravity, following the drawings from BSHC (Milanov 2010).

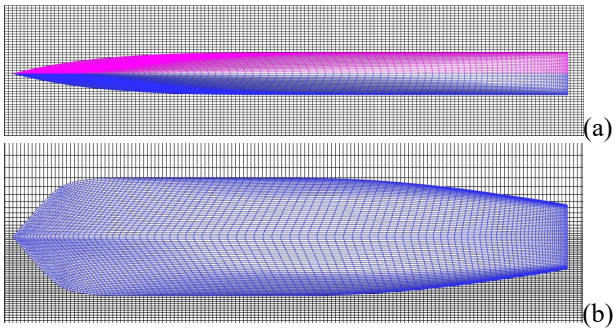

Figure 4: Bare hull grid system: (a) bottom view, (b) side view.

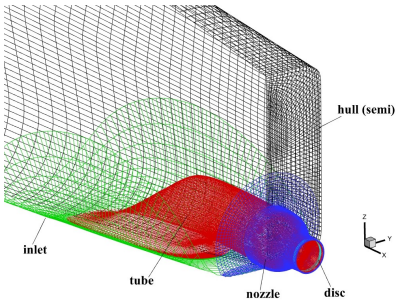

Figure 5: Overset grids for the self-propulsion cases.

3.3.2 Free Running Self-Propulsion Simulation Setup

For high-fidelity self-propulsion simulations, the waterjet system is included in the geometry, as shown in Figure 5. The same Cartesian background and bare hull grids are used with additional grids for the waterjet system, as shown in Table 1. No-slip wall boundary conditions are imposed on the surface of the waterjet system. The time step used is the same as that employed in captive simulations. The CFL number is maintained at 0.9 in most areas except for the nozzle region, where a finer grid is employed, resulting in a CFL number of up to 4.2. An implicit time integration method is utilized in the calculations, enabling the use of a large time step. Note that the center of gravity (CG) and displacement for bare hull are available in the experiment reports and previous CFD studies. However, they are not clearly defined for the self-propulsion cases. The sinkage and trim are very sensitive to the CG and displacement, and a series of numerical experiments have been conducted using various CG and displacement values. In the present work, the CG used for the self-propulsion is the same as used by Zou et al (2023), and the displacement is reduced by 2.7% compared with the bare hull due to the opening of the waterjet inlet.

For low-fidelity self-propulsion simulations, the geometry of the waterjet system is not included, and the grid is the same as the captive simulations, as summarized in Table 2.

Table 1: Grid details for captive and self-propulsion simulations.

Bare hull		
Block #	Description	# grid points
1	Inner-hull	401,380
2	Outer-hull	401,380
3	Background	4,391,288
Total		5,194,048
Bare hull + WJ system		
1	Inner-hull	401,380
2	Outer-hull	401,380
3	Inlet	173,264
4	Tube	1,449,420
5	Disc	68,544
6	Bat	48,790
7	Nozzle	948,192
8	Background	4,391,288
Total		7,882,258

Table 2: CFD simulation setup

Cases	Geometry	Propulsion
Captive	BH	-
Self-propulsion	BH+WJ	HF
	BH	LF
Fixed sinkage/trim	BH	-

3.4 Analysis Methods: ITTC Momentum Flux and Integral Methods

The self-propulsion simulation results are analyzed using the ITTC momentum flux and integral methods. ITTC developed the momentum flux method (Van Terwisga 2005) to analyze experimental results on the Athena semi-planing hull with two waterjets. This method is based on the evaluation of momentum and energy fluxes over characteristic sections of the waterjet system. It is relatively easy to apply to experimental studies, and its usage can also be found in previous CFD studies. The accuracy of the analysis using the momentum flux method significantly depends on the accuracy of the calculated flow rate.

The integral method (Dogan et al 2022) is based on the integration of the stresses on the hull and waterjet surfaces. The delivered power, gross thrust, and waterjet efficiency can be calculated using this method. Figure 6 displays the division of hull and waterjet surfaces for the DC. Details of the methods can be found in the above papers.

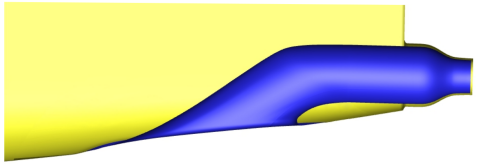

Figure 6: Division between hull and waterjet system in the integral method.

4 RESULTS AND DISCUSSION

4.1 Captive Simulations

Figure 7 shows a comparison of the wave patterns around the hulls for $Fr = 0.3$ and $Fr = 0.7$. The water surface near the stern shows significant differences, with a large drop for $Fr = 0.7$. The comparison of the EFD and CFD resistance is presented in Figure 8, and the sinkage and trim are shown in Figure 11. Bare hull simulations are conducted for $Fr = 0.3, 0.4, 0.5, 0.6$, and 0.7, corresponding to a towing speed range of $1.79m/s$ to $4.18m/s$. Overall, the simulation results show good agreement with the experimental data provided by BSHC and INSEAN and the prediction errors are presented in Table 3. The CFD sinkage prediction exhibits a substantial error at $Fr = 0.7$, whereas other speeds demonstrate good agreement and the average error is $43.32\%D$. Dogan (2013) also shows a similar trend for high Fr simulations using CFDShip-Iowa. The trim angle aligns well with the experimental data, except for $Fr = 0.5$, where a peak results in a larger error. The bare

hull resistance shows very close agreement with EFD data, with $E = 3.83\%D$.

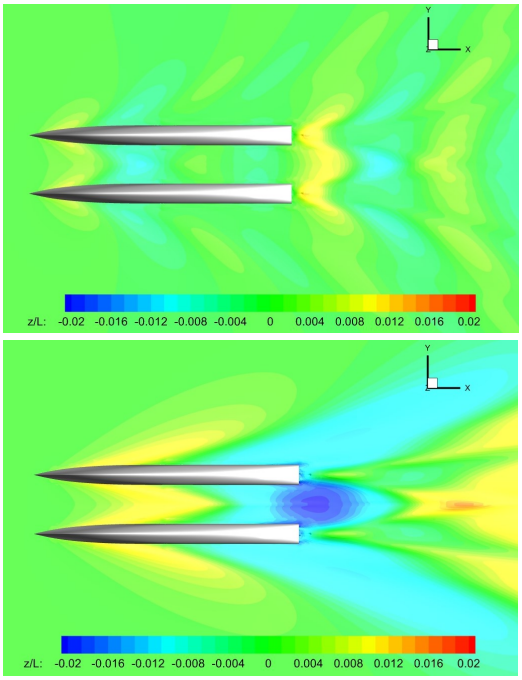

Figure 7: Comparison of free surface elevation, captive simulations: (a) $Fr = 0.3$, (b) $Fr = 0.7$.

Table 3: Prediction errors of captive CFD simulations.

	$E\%$ Mean EFD		
Fr	R_{BH}[N]	$\sigma/L \times 10^{-3}$ [-]	τ [deg]
0.30	5.46	8.77	82.23
0.40	-2.17	9.70	3.10
0.50	8.42	7.02	20.17
0.60	2.17	-0.66	4.85
0.70	-0.93	-190.44	-3.35
Mean	3.83	43.32	22.74

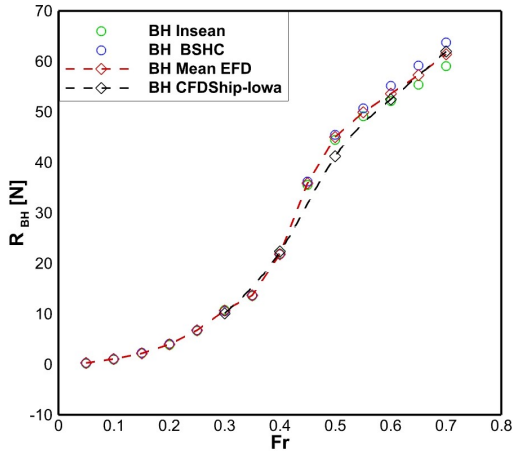

Figure 8: EFD and CFD comparison of hull resistance for captive cases.

4.2 High-Fidelity Self-Propulsion Simulations

Self-propulsion simulations are conducted for $Fr = 0.3$, 0.4, 0.5, 0.6, and 0.7, and comparison of wave patterns between captive and self-propulsion simulations at $Fr = 0.3$ and 0.5 is shown in Figure 9. The suction force due to the waterjet induces a drop in the free surface around the inlet region, thereby altering the pressure distribution along the hull, as demonstrated in Figure 10. A low-pressure area around the inlet is also generated, resulting in increased hull submersion and a subsequent rise in the trim angle.

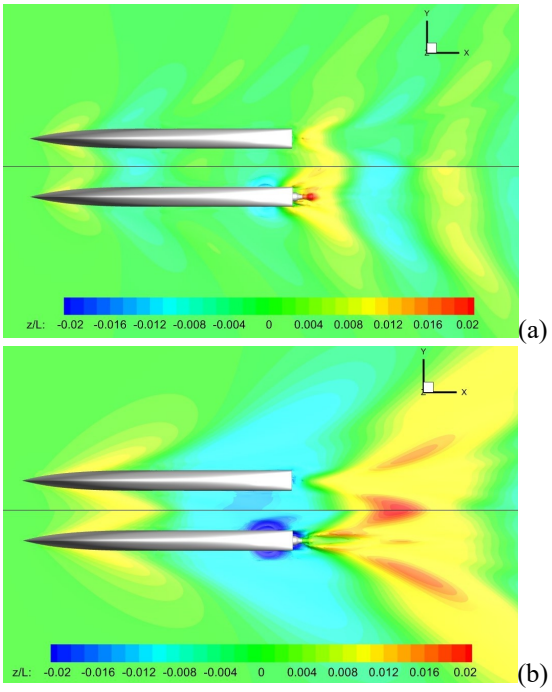

Figure 9: Comparison of free surface elevation between captive and self-propulsion simulations: (a) $Fr = 0.3$, (b) $Fr = 0.5$.

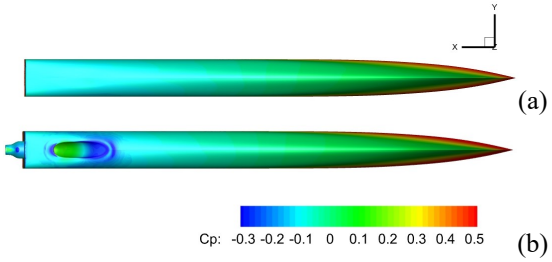

Figure 10: Pressure coefficient distribution at $Fr = 0.5$: (a) captive, (b) self-propulsion.

The results for sinkage, trim, delivered power, and gross thrust are presented in Figure 11, with the prediction errors shown in Table 4. Overall, the simulations align with the trends observed in the experiments. Both sinkage and trim are overpredicted for $Fr = 0.6$ and 0.7 and the average error is $33.82\%D$ and $16.22\%D$, respectively. In the experiment, a towing post is used to execute the self-propulsion test, whereas CFD simulations are carried out using free running conditions. This might be one of the reasons for

the large differences at high Fr. A systematic grid verification study will be carried out in future work to evaluate the grid resolution effect on the scatter of numerical results.

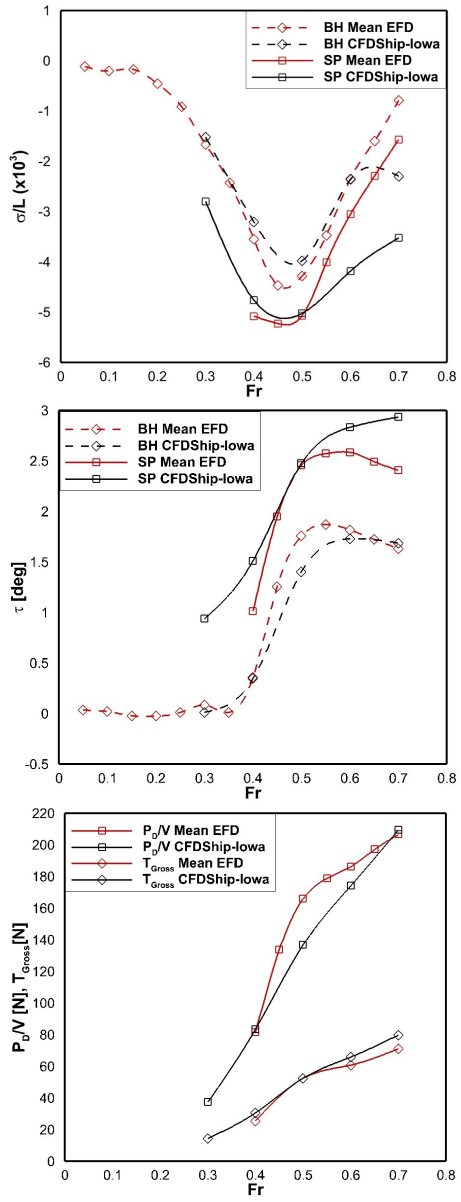

Figure 11: EFD and CFD comparison for self-propulsion cases: (a) sinkage, (b) trim angle, (c) delivered power and gross thrust.

The delivered power from the simulations is calculated directly from the body-force thrust and generally shows good agreement with an average error of 5.53%D. The gross thrust is evaluated using the momentum flux difference between the nozzle section and the capture area, following ITTC recommendations (Van Terwisga 2005). Simulation results show an overestimation of the gross thrust with an error of $E = 8.03\%D$. The discrepancy is attributed to the overestimated flow rate in the CFD results, as depicted in Figure 12. The high flow rate leads to additional momentum flux in both the capture area and the nozzle section of the waterjet. The elevated flow speed at the nozzle, which is associated with a larger momentum flux, contributes to the higher gross thrust output. Therefore, the overestimated flow rate directly influences the observed increase in the gross thrust.

Table 4: Prediction errors of high-fidelity self-propulsion CFD.

	E% Mean EFD				
Fr	0.40	0.50	0.60	0.70	Mean
P_D/V $[N]$	-2.12	17.62	6.47	-1.46	5.53
T_{Gross} $[N]$	-19.65	-0.18	-8.34	-12.21	8.08
σ/L $\times 10^{-3}$	6.26	0.92	-36.98	-124.93	33.82
$\tau[deg]$	-48.98	-0.68	-9.52	-21.91	16.22

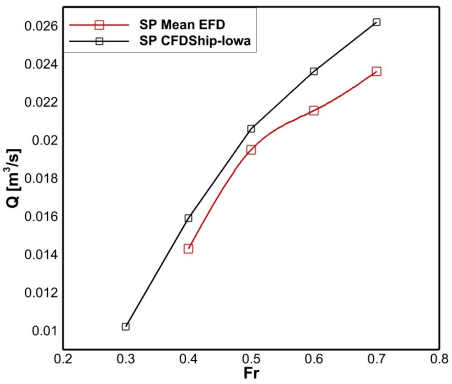

Figure 12: EFD and CFD flow rate comparison.

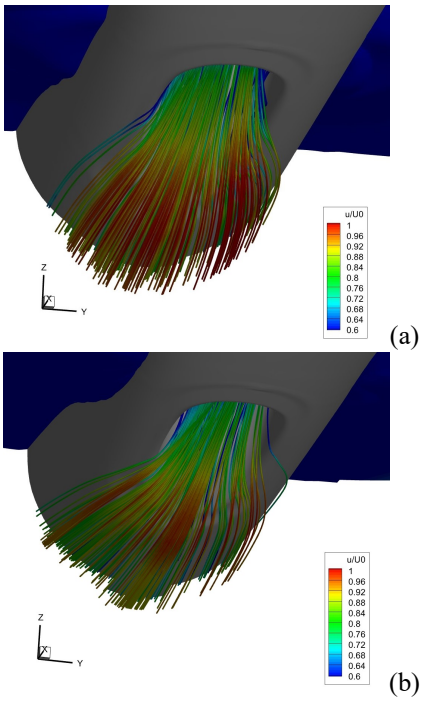

Figure 13: Capture area: (a) $Fr = 0.4$, (b) $Fr = 0.7$.

Figure 13 shows the CFD capture area obtained by tracing

the streamlines entering the duct. As shown in other studies (Takai et al 2011; Kandasamy et al 2011; Zou et al 2023), the capture area has an elliptical shape and it is placed one inlet diameter in front of the intake tangency point (Van Terwisga 2005).

Since the momentum flux method relies on an accurate determination of the flow rate, a correction is applied in the evaluation of the thrust and power for the waterjet system (Dogan et al 2022). P_{JSE} and P_{PE} are directly proportional to the cube of the flow rate, whereas P_{TE} is proportional to the square. The corrected quantities are evaluated as:

$$P_{JSE_c} = P_{JSE}\left(\frac{Q_{EFD}}{Q_{CFD}}\right)^3 \quad (3)$$

$$P_{PE_c} = P_{PE}\left(\frac{Q_{EFD}}{Q_{CFD}}\right)^3 \quad (4)$$

$$P_{TE_c} = P_{TE}\left(\frac{Q_{EFD}}{Q_{CFD}}\right)^2 \quad (5)$$

This correction takes into account the flow rate overprediction of the CFD simulations, to obtain a more meaningful comparison with EFD data. Results of the momentum flux and integral analysis are presented in Figure 14 and Table 5. Both the momentum flux and integral method show larger values than EFD for η_{wj}, whereas the predictions for the thrust deduction factor are similar to the experimental results. The pump efficiency calculated using the momentum flux method is 30.57%D larger than experimental values. However, application of the flow rate correction decreases the error to 11.05%D. The overprediction of the flow rate determines a larger value for the pump power, which causes an increase in the pump efficiency. Similarly, the waterjet efficiency error is largely reduced when the flow rate correction is applied. The system efficiency η_D is evaluated as the ratio of the bare hull resistance over the body force thrust and presents a 7.84%D error for both the momentum flux and integral method.

Table 5: Comparison of momentum flux and integral analysis.

η	Method		E% Mean EFD				
Fr			0.40	0.50	0.60	0.70	Avg.
η_{pump}	MF	O	-30.4	-45.4	-28.7	-17.8	30.6
		C	5.84	-22.6	1.54	14.2	11.1
$\eta_{\text{jet}} \times \eta_{\text{duct}}$	MF	O	9.59	16.1	9.94	5.96	10.4
		C	-0.78	11.2	1.54	-4.52	4.50
η_{wj}	MF	O	-17.9	-22.0	-15.9	-10.81	16.7
		C	5.10	-8.93	3.05	10.3	6.85
	INT		-41.1	-31.5	-19.9	-11.2	25.9
$1-t$	MF	O	16.4	0.23	7.72	11.0	8.85
		C	-3.84	-11.8	-10.3	-9.91	8.95
	INT		29.3	6.90	10.6	10.9	14.4
η_{D}	MF/INT		1.39	-21.7	-6.88	1.37	7.84

Note: MF=Momentum flux, INT=Integral, O=Original, C=Corrected

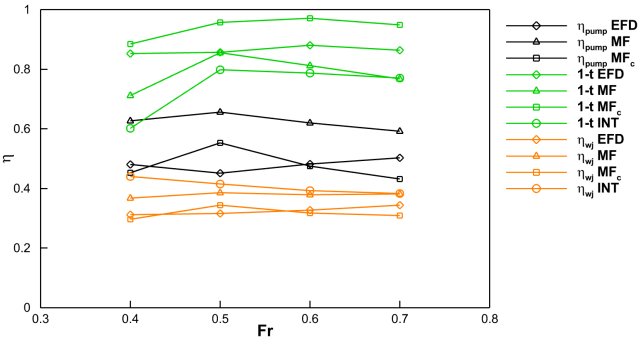

Figure 14: Results of momentum flux and integral method: waterjet efficiencies.

4.3 Low-Fidelity Self-Propulsion Simulations

Figure 15 shows F_Z and M_{WJ} obtained from the hydrostatic correlations (Eqs. 1 and 2) and direct method using CFD simulations with prescribed sinkage and trim.

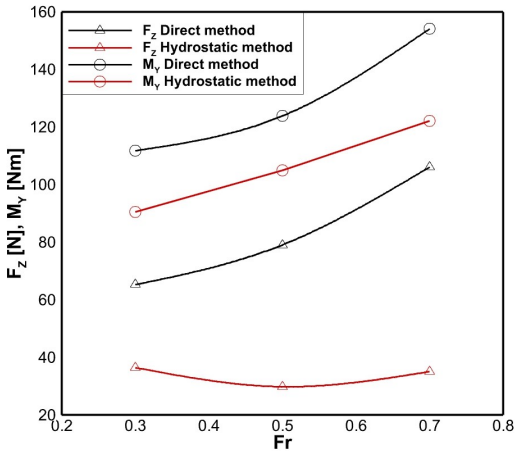

Figure 15: Vertical force and pitch moment results for direct and hydrostatic model.

Both methods are trained based on $Fr = 0.3, 0.5, 0.7$ simulations and $Fr = 0.4, 0.6$ results are obtained using interpolation. The pitch moment shows a similar trend for the two methods, and the direct method shows larger values. F_Z force shows a very different trend for the two methods, which only slightly changes with Fr for the hydrostatic method.

Self-propulsion simulations are carried out using the low-fidelity propulsion model with the input obtained from the two different methods. The sinkage and trim are presented in Figure 16. As shown in the figure, the direct method shows very good agreement with the HF self-propulsion simulations for both sinkage and trim, with an average error of 5.22%D and 4.94%D, respectively, compared with high-fidelity self-propulsion data. The hydrostatic model shows good agreement for the trim, but it severely underpredicts the sinkage with $E = 40.06\%D$, due to the lower value of the vertical force applied on the hull. By using the system efficiency η_D, the point-force F_x used to propel the hull is related to the delivered power of the

self-propulsion showing an average error of 7.33%D and 7.12%D for the hydrostatic and direct model, respectively. Moreover, the computational speed is increased by up to 8 times as compared to the high-fidelity self-propulsion simulations in terms of the wall-time.

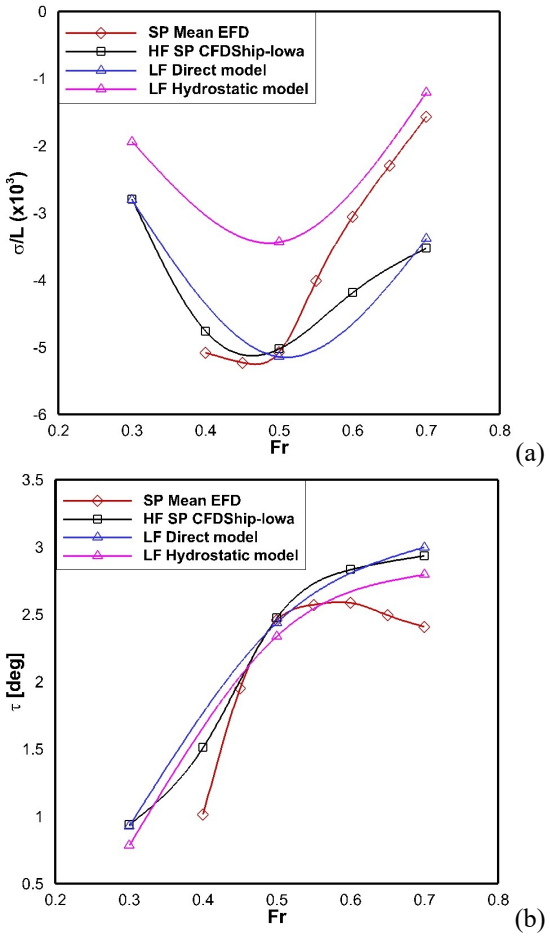

Figure 16: Low-fidelity models results: (a) sinkage, (b) trim angle.

5 CONCLUSIONS AND FUTURE RESEARCH

In this study, multi-fidelity modeling of the Delft catamaran is performed using CFDShip-Iowa V4.5 including captive, self-propulsion, and prescribed trim and sinkage simulations. High-fidelity simulations are conducted first to verify the computational setup and validate the computational results against experimental measurements. A low-fidelity force and moment propulsion model is implemented based on the high-fidelity simulation results and a hydrostatic approximation correlation, which is applied to self-propulsion simulations. The simulation results are analyzed using ITTC momentum flux and integral methods.

For the high-fidelity simulations, the captive simulation results show good agreement with the EFD except for high Fr cases. The waterjet causes the drop of the water surface near the inlet location, which reduces the pressure at the bottom of the hull near the stern. Both sinkage and trim of the hull are increased as compared to the captive cases. The overpredicted flow rate is corrected to evaluate the thrust and power for the waterjet system, and reasonable agreement with the EFD is obtained.

The low-fidelity propulsion model trained based on the high-fidelity computational data shows better simulation results (errors less than 5%D) than using the hydrostatic approximation correlation. The computations are accelerated by a factor of up to 8 using the low-fidelity model.

It should be noted that the pump curve used for the high-fidelity self-propulsion simulations is based on the experimental data, only available for high J values (0.8), which will affect the accuracy of the predicted flow rate and RPS since the J value used in the present simulations is around 0.61. The CG and displacement for the bare hull are well documented in the literature, however, they are not clearly defined for the self propulsion cases, which significantly affects the sinkage and trim.

In the future work, a low-fidelity model for maneuvering conditions will be developed. New experiments will be carried out at IIHR Wave Basin to refine the CFD setup (tow point, displacement, and CG location). A systematic grid verification study will be performed to investigate the sensitivity of the numerical results to grid resolution. Extension to different hulls especially for waterjet propelled GPPH will be made. The multi-phase flow solver, CFDShip-Iowa V5.5 (Wang and Stern 2022, 2023), will also be used for more accurate modeling of air-water interfacial flows.

ACKNOWLEDGEMENTS

This work is supported by the Office of Naval Research grants N00014-20-1-2259 and N00014-22-1-2413 under the administration of Dr. Robert Brizzolara. The simulations were performed using DoD DSRC HPCMP resources, including FY23 Pathfinder program allocations.

REFERENCES

Bell, J., Howell, L. & Colella, P. (1991). 'An efficient second-order projection method for viscous incompressible flow'. Proceedings of the 10th Computational Fluid Dynamics Conference , Honolulu, Hawaii.

Carrica, P. M., Wilson, R. V., Noack, R. W. & Stern, F. (2007a). 'Ship motions using single-phase level set with dynamic overset grids'. Computers & Fluids **36**(9), pp. 1415–1433.

Carrica, P. M., Wilson, R. V. & Stern, F. (2007b). 'An unsteady single-phase level set method for viscous free surface flows'. International Journal for Numerical Methods in Fluids **53**(2), pp. 229–256.

Dogan, T., Sadat-Hosseini, H. & Stern, F. (2022). 'Effects of Hook, Interceptor, and Water Jets on LCS Resistance/Power, Sinkage, and Trim'. Journal of Ship Research **66**(2), pp. 127–150.

Dogan, T. K. (2013). Urans and des for delft catamaran for static drift conditions in deep water.

Huang, J., Carrica, P. M. & Stern, F. (2007). 'Coupled ghost fluid/two-phase level set method for curvilinear body-fitted grids'. International Journal for Numerical Methods in Fluids **55**(9), pp. 867–897.

Huang, J., Carrica, P. M. & Stern, F. (2008). 'Semi-coupled air/water immersed boundary approach for curvilinear dynamic overset grids with application to ship hydrodynamics'. International Journal for Numerical Methods in Fluids **58**(6), pp. 591–624.

Kandasamy, M., Georgiev, S., Milanov, E. & Stern, F. (2011). 'Numerical and experimental evaluation of waterjet propelled delft catamarans'.

Kandasamy, M., Ooi, S. K., Carrica, P. & Stern, F. (2010). 'Integral Force/Moment Waterjet Model for CFD Simulations'. Journal of Fluids Engineering **132**(10), pp. 101–103.

Kandasamy, M., Peri, D., Tahara, Y., Wilson, W., Miozzi, M., Georgiev, S., Milanov, E., Campana, E. & Stern, F. (2013). 'Simulation based design optimization of waterjet propelled Delft catamaran'. International Shipbuilding Progress **60**(1-4), pp. 277–308.

Menter, F. R. (1994). 'Two-equation eddy-viscosity turbulence models for engineering applications'. AIAA Journal **32**, pp. 1598–1605.

Milanov, E. (2010). Model tests of waterjet propelled delft 372 catamaran. Technical Report KP092006/01, BSHC.

Milanov, E., Chotukova, V., Efremov, D. & Stern, F. (2014). 'Systematic experimental investigation of maneuvering characteristics of free running delft catamaran in still water and regular waves'. Proceedings of the 30th Symposium on Naval Hydrodynamics , Hobart, Australia.

Miozzi, M. (2011). Model tests of waterjet propelled delft 372 catamaran. Technical Report 2011-TR-011, INSEAN-CNR.

Noack, R. (2005). 'SUGGAR: A general capability for moving body overset grid assembly'. Proceedings of the 17th AIAA computational fluid dynamics conference , Toronto, Canada.

Sadat-Hosseini, H., Chen, X., Kim, D., Milanov, E., Georgiev, S., Zlatev, Z. & Stern, F. (2013). 'Cfd and system-based prediction of delft catamaran maneuvering and course stability in calm water'. Proceedings of the Proceedings of 12th International Conference on Fast Sea Transportation , Amsterdam, The Netherlands.

Stern, F., Diez, M., Wang, Z., Lee, E. J. & Kubina, E. R. (2022). 'Digital Design: The Way Forward'. Proceedings of the AVT-366 Research Workshop , Sibiu, Romania.

Stern, F., Kim, H. T., Patel, V. C. & Chen, H. C. (1988). 'A Viscous-Flow Approach to the Computation of Propeller-Hull Interaction'. Journal of Ship Research **32**(04), pp. 246–262.

Stocker, M., Sanada, Y. & Stern, F. (2014). 'Preliminary Free-running Test of the Delft Catamaran Waterjet Model'. Naval Engineers Journal (126-4), pp. 169–172.

Takai, T., Kandasamy, M. & Stern, F. (2011). 'Verification and validation study of urans simulations for an axial waterjet propelled large high-speed ship'. Journal of Marine Science and Technology **16**(4).

Van Terwisga, T. (2005). 'Report of the specialist committee on validation of waterjet test procedures'. Proceedings of the 24th International Towing Tank Conference, volume 2 , Edinburgh, UK.

Van't Veer, R. (1998). Experimental results of motions, hydrodynamic coefficients and wave loads of the 372 catamaran model. Technical report, TUDelft, Faculty of Marine Technology.

Wang, Z. & Stern, F. (2022). 'Volume-of-fluid based two-phase flow methods on structured multiblock and overset grids'. International Journal for Numerical Methods in Fluids **94**(6), pp. 557–582.

Wang, Z. & Stern, F. (2023). 'Moving contact line and no-slip boundary conditions for high-speed planing hulls'. Proceedings of the X International Conference on Computational Methods in Marine Engineering, MARINE 2023 , Madrid, Spain.

Zou, Y., Feng, D., Deng, W., Yang, J. & Zhang, H. (2023). 'Numerical study on the waterjet-hull interaction of a free-running catamaran'. Journal of Marine Science and Engineering **11**(4).